JOURNAL OF COMPUTATIONAL PHYSICS 68, 346–377 (1987)

Vortex Simulation of Laminar Recirculating Flow

AHMED F. GHONIEM AND YVES CAGNON

Department of Mechanical Engineering, Massachusetts Institute of Technology, Cambridge, Massachusetts 02139

Received October 25, 1985; revised March 5, 1986

The accuracy of the random vortex method, a numerical scheme that combines the representation of the vorticity field by a number of Lagrangian vortex elements of finite cores with a stochastic simulation of diffusion using random walk, is investigated. The converged solutions for a 2-dimensional entry flow in a channel and a recirculating flow behind a rearward-facing step, both in the laminar range of Reynolds numbers, are compared with analytical results and experimental data, respectively. It is shown that the computed results converge as the strength of computational vortex elements is decreased, and that the method is accurate to within the experimental errors. The convergence properties are used to devise a scheme for optimizing the choice of the numerical parameters.

1. INTRODUCTION

Vortex methods have been used to construct numerical solutions for the Navier–Stokes equations at high Reynolds numbers, and to model the development of unstable flow fields associated with the roll-up of velocity discontinuities. The success of vortex methods in the second task was achieved after employing a filtering mechanism to remove the numerical instability associated with the use of singular point vertices (Chorin and Bernard [1], Kuwahara and Takami [2], Saffman and Baker [3]). In particular, the use of vortex elements with finite cores was essential to avoid the irregular motion that develops after the amplitude of the instability wave reaches a maximum, and to allow the successive roll-ups of the instability to continue in an organized form (Krasny [4]). In this paper, we show that vortex methods can be used to accomplish the first task successfully. Attention is focused on steady solutions.

Vortex methods present a promising candidate for numerical simulation of unsteady flows. The representation of the vorticity field by a number of vortex elements is the most natural way to overcome the difficulties associated with the convective non-linearity of the Navier–Stokes equations. By employing a Lagrangian formulation, convection is expressed in terms of a set of coupled ordinary differential equations that can be integrated using efficient and accurate schemes. The numerical diffusion is minimized by avoiding the discretization of gradients. The Lagrangian scheme is grid-free, and the computations are self-adaptive since vortex elements move to capture zones of large gradients associated with high concentrations of vorticity.

0021-9991/87 $3.00

The development of numerical schemes for the solution of the Navier–Stokes equations requires, in addition to the representation of the vorticity field by a number of non-singular vortex elements, the implementation of two extra mechanisms: (1) The satisfaction of the no-slip boundary condition along solid boundaries; and (2) the transports of vortex elements by diffusion. For that purpose, Chorin [5, 6, 7] proposed the random vortex method, in which vortex blobs are continuously generated along solid boundaries by satisfying the no-slip condition, and transported in the interior by convection and diffusion in a Langrangian fashion. The latter is simulated by the random walk displacement of the vortex elements according to Gaussian statistics. The vortex sheet algorithm was introduced to simulate the boundary layer flow, and was used to satisfy the no-slip condition in the original scheme.

The random vortex method was applied to the recirculating flow behind a rearward-facing step at high Reynolds numbers by Ashurst [8] and by Ghoniem, Chorin, and Oppenheim [9]. The computed results showed good qualitative agreement with experimental observations in terms of the structure of the vorticity field and its unsteady dynamics. No attempt was made to compare the computed velocity field with the experimental measurements since the actual flow was turbulent, hence 3-dimensional, while the numerical solution was based on the assumption that the flow is strictly 2-dimensional. Three-dimensional effects at high Reynolds numbers were manifested in the results of Hsiao *et al.* [10]; although the average velocity profiles were accurately computed, the fluctuating components of the velocity were poorly predicted. Cheer [11] presented a study for a high Reynolds number flow around an impulsively started cylinder.

The discrepancy between the flow model used in the numerical study and the observed behaviour of the actual flow makes comparison between numerical results and experimental data inconclusive insofar as the accuracy of the scheme is concerned. As shown by Ghoniem and Sethian [12], and Sethian and Ghoniem [13], computations at low Reynolds numbers, where the actual flow is 2-dimensional, should be performed to investigate systematically the numerical errors. Quantitatively, similarity between the numerical results and experimental observations on the structure of the recirculation zone, reported in [12, 13], showed that the random vortex method is sensitive to the changes in the dynamics of the flow from viscous-dominated to a balance between viscous and inertia forces. In the present paper, the accuracy of the method is investigated quantitatively by comparing computed results for an entry flow in a channel and for a recirculating flow behind a rearward-facing step with analytical and experimental results, respectively, at moderate Reynolds numbers.

Convergence analysis of inviscid vortex methods have revealed valuable insight into their properties. Hald [14] proved that the solution obtained by an inviscid vortex scheme converges to the solution of the Euler equations if the numerical parameters are chosen appropriately. His analysis emphasized that the rate of convergence of the scheme depends on the form of the core function, and the ratio between the core radius and the initial separation between vortex elements. Beale

and Majda [15] were able to construct a class of core functions that produces arbitrary high order schemes. In both cases, the flow field extended to infinity and the total vorticity was constant, while the time integration of the ordinary differential equations that govern the convective motion of vortex elements was exact. Anderson and Greengard [16] amended the analysis to include the effect of a finite order time integration scheme. Numerical experiments were conducted by Nakamura *et al.* [17] to verify these results for inviscid flows.

Ghoniem and Sherman [18] extended the random walk algorithm for the simulation of diffusion to solve the problem of natural convection over an infinite flat plate in one dimension. In this scheme, vorticity is continuously generated inside the field by the action of the baroclinic torque, and at the wall by the satisfaction of the no-slip condition. The latter resembles the methodology of satisfying the boundary condition in the random vortex method. Computed results showed good agreement with the analytical solution of the same problem. Hald [19] established the convergence of this scheme, showing that the error is independent of the viscosity.

In this work, the convergence and accuracy of the random vortex method is investigated computationally by conducting careful numerical experiments on two flow fields: entry flow in a channel and recirculating flow behind a rearward-facing step. The analytical solution of the first flow and the experimental results for the second flow are used for comparison. In both cases, flow fields are computed at a range of the Reynolds number where experimental observations indicate that the flow is free of 3-dimensional effects. Because of the lack of unsteady solutions or measurements for either flows, we concentrate on steady solutions. We define an accurate solution as a solution that is close to the analytical solution or to the experimental results, and a convergent solution as a solution that becomes more accurate as the numerical parameters are defined. An optimum solution is one which is accurate, while it is obtained with the minimum computational effort. A criterion is suggested for the sufficient number of vortex elements to obtain an accurate solution.

In Section II, the formulation of the scheme is presented. In particular, we show how the potential and the no-slip boundary conditions are satisfied, and what are the numerical parameters that control the accuracy of the scheme. In Section III, results are presented for an entry channel flow and a recirculating flow. In Section IV, the effect of changing the controlling numerical parameters is analyzed. Section V is devoted to brief conclusions.

II. Formulation and Numerical Scheme

The dynamics of a 2-dimensional incompressible flow is governed by the conservation of mass and momentum. In terms of the velocity and pressure, the differential equations and boundary conditions are

$$\nabla \cdot \mathbf{u} = 0 \tag{1}$$

$$\frac{\partial \mathbf{u}}{\partial t} + \mathbf{u} \cdot \nabla \mathbf{u} = -\nabla p + \frac{1}{R} \Delta \mathbf{u} \tag{2}$$

$$\mathbf{u} = 0 \qquad \text{on} \quad \partial_w D, \tag{3-a}$$

$$\mathbf{u} = (1, 0) \qquad \text{on} \quad \partial_i D, \tag{3-b}$$

where $\mathbf{u} = (u, v)$ is the velocity normalized with respect to the uniform velocity at the inlet section of the channel U; $\mathbf{x} = (x, y)$, x and y are the streamwise and cross-stream directions, respectively, both normalized with respect to a reference length H_s, where H_s is the step height. t is the time normalized with respect to H_s/U, p is the pressure normalized with respect to ρU^2 and the Reynolds number $R = \rho U H_s/\mu$, where ρ is the density and μ is the viscosity, while

$$\nabla = \left(\frac{\partial}{\partial x}, \frac{\partial}{\partial y} \right) \qquad \text{and} \qquad \Delta = \frac{\partial^2}{\partial x^2} + \frac{\partial^2}{\partial y^2}.$$

D is the solution domain, ∂D is the boundary such that $\partial_w D$ is the walls and $\partial_i D$ is the inlet section. The outlet boundary condition will be presented in a later section. Vorticity is defined as the curl of the velocity vector, $\boldsymbol{\omega} = \nabla \times \mathbf{u}$. In two dimensions, $\boldsymbol{\omega}$ is the scalar:

$$\omega = \frac{\partial v}{\partial x} - \frac{\partial u}{\partial y}. \tag{4}$$

The vorticity transport equation is derived by taking the curl of Eq. (2). Using Eq. (1) and the identity $\nabla \times \nabla p = 0$, one obtains the following equation:

$$\frac{\partial \omega}{\partial t} + \mathbf{u} \cdot \nabla \omega = \frac{1}{R} \Delta \omega \tag{5}$$

expressing the transport of vorticity by convection and diffusion. Knowing the vorticity field, the velocity can be evaluated by integrating Eqs. (1) and (4), and using Eq. (5), the vorticity field can be advanced in time. The pressure is recovered from the velocity field by integrating the following equation:

$$\Delta p = 2 \left(\frac{\partial u}{\partial x} \frac{\partial v}{\partial y} - \frac{\partial u}{\partial y} \frac{\partial v}{\partial x} \right) \tag{6}$$

which is derived as the divergence of Eq. (2) and using Eq. (1).

In vortex methods, Eq. (5) is solved in two fractional steps by implementing the two mechanisms of transport in each time step of the computations individually such that

$$\frac{\partial \omega}{\partial t} + \mathbf{u} \cdot \nabla \omega = 0 \tag{7}$$

$$\frac{\partial \omega}{\partial t} = \frac{1}{R} \Delta \omega. \tag{8}$$

In the first fractional step, the transport of vorticity due to convection is obtained from the solution of Eq. (7) in terms of the Lagrangian displacement of a set of finite vortex elements. In the second step, the solution of Eq. (8) is simulated stochastically by the random walk displacement of the same vortex elements. The boundary conditions, Eqs. (3), are satisfied by adding a potential velocity field in the convection step, and by creating extra vortex elements to satisfy the no-slip condition in the diffusion step. In the following, we describe each step in more detail.

II.1. *Convection*

Equation (1) is satisfied by using a stream function ψ such that

$$u = \frac{\partial \psi}{\partial y} \qquad \text{and} \qquad v = -\frac{\partial \psi}{\partial x}. \tag{9}$$

Substituting into Eq. (4), the following Poisson equation is obtained:

$$\Delta \psi = -\omega(\mathbf{x}). \tag{10}$$

The solution of this equation in a domain without boundaries is given in terms of the Green function of the Poisson equation as

$$\psi(\mathbf{x}) = \int G(\mathbf{x} - \mathbf{x}')\, \omega(\mathbf{x}')\, d\mathbf{x}' \tag{11}$$

where

$$G(\mathbf{x}) = -\frac{1}{2\pi} \ln r.$$

$r^2 = x^2 + y^2$, $d\mathbf{x} = dx\, dy$, and the integration is performed over the area where $|\omega| > 0$. The velocity distribution is recovered by substituting Eq. (11) into Eq. (9):

$$\mathbf{u}(\mathbf{x}) = \int K(\mathbf{x} - \mathbf{x}')\, \omega(\mathbf{x}')\, d\mathbf{x}' \tag{12}$$

where

$$\mathbf{K}(\mathbf{x}) = -\frac{1}{2\pi} \frac{(y, -x)}{r^2}. \tag{13}$$

$\mathbf{K}$ is the integral kernel of the Poisson equation. If $\chi(\mathbf{X}, t)$ is the trajectory of a par-

ticle that starts at $\mathbf{X}$, and $\omega(\mathbf{X})$ is the vorticity distribution at $t=0$, then Eq. (7) is equivalent to (by virtue of Kelvin–Helmholtz theorem)

$$\omega(\chi(\mathbf{X}, t)) = \omega(\mathbf{X}) \tag{14}$$

while χ is the solution of the differential equation:

$$\frac{d\chi}{dt} = \mathbf{u}(\chi(\mathbf{X}, t)) \qquad \text{and} \qquad \chi(\mathbf{X}, 0) = \mathbf{X}\,. \tag{15}$$

Using this Lagrangian formulation of the vorticity transport equation circumvents the difficulties associated with the numerical treatment of the non-linearity of the inertial terms in the Navier–Stokes equations. It also allows the construction of efficient grid-free schemes in which the computational points follow the vorticity field in time.

Equation (15) is a set of uncountably many ordinary differential equations which, supplemented with Eq. (12), provides a solution for the inviscid part of the Navier–Stokes equations. In order to reduce this to a finite number of equations, $\omega(\mathbf{X})$ is discretized among small area elements to form particles of vorticity, or vortex blobs, each carrying a finite and invariant circulation Γ. The area A where $|\omega| > 0$ is divided into a number N of adjointed area elements δA_i and the circulation assigned to each vortex element is calculated as

$$\begin{aligned} \Gamma_i &= \int_{\delta A_i} \omega(\mathbf{X})\, d\mathbf{X} \\ &\cong \omega(X_i)\, \delta A_i. \end{aligned} \tag{16}$$

The vorticity carried by each blob is distributed according to a core function with a finite radius δ (Chorin and Bernard [1], and Kuwahara and Takami [2]). Within the core, vorticity is smooth, or almost smooth, guaranteeing a finite velocity at the center of the vortex element. The resulting approximation of the vorticity distribution is

$$\omega(\mathbf{x}) = \sum_{i=1}^{N} \Gamma_i f_\delta(\mathbf{x} - \chi_i). \tag{17}$$

f_δ is the core function; it is radially symmetric, $f = f(r)$, while $\int f_\delta\, d\mathbf{x} = 1$. δ represents the characteristic fall-off length such that f_δ is small, or $f_\delta = 0$ for $r > \delta$. In order to approximate the initial vorticity distribution accurately, 2δ is often chosen to be larger than the initial separation between vortex centers such that a margin of overlap is allowed between vortex elements. In a normalized form, f_δ can be written as

$$f_\delta(r) = \frac{1}{\delta^2} f\left(\frac{r}{\delta}\right). \tag{18}$$

The core function f plays a similar role as interpolating polynomials in finite-difference schemes and base functions in finite-element formulations. By requiring f to be radially symmetric, the approximation in Eq. (17) is at least second order (Hald [20].)

The velocity produced by a distribution of finite-core vortex blobs is obtained by substituting Eq. (17) into Eq. (12):

$$\mathbf{u}_\delta(\mathbf{x}) = \sum_{i=1}^{N} \Gamma_i \mathbf{K}_\delta(\mathbf{x} - \boldsymbol{\chi}_i) \tag{19}$$

where

$$\mathbf{K}_\delta(\mathbf{x}) = -\frac{1}{2\pi} \frac{(y, -x)}{r^2} \kappa\left(\frac{r}{\delta}\right) \tag{20}$$

and

$$\kappa(r) = 2\pi \int_0^r r f(r)\, dr\,; \tag{21}$$

κ represents the fractional circulation of the element within radius r. A choice of f that has been used extensively in applications is the function suggested by Chorin [5], for which

$$f(r) = \begin{cases} 1/(2\pi r) \\ 0 \end{cases} \quad \text{and} \quad \kappa(r) = \begin{cases} r & \text{for } r \leqslant 1, \\ 1 & \text{for } r > 1. \end{cases} \tag{22}$$

This is the simplest choice. While it possesses a singularity in the vorticity distribution and a discontinuity in the velocity field, it has been used in numerous studies because of its comptability with the vorticity generation algorithm at the walls (McCraken and Peskin [21], Ghoniem *et al.* [10], Cheer [11], Sethian [22], Ghoniem and Sethian [12]; see also Acton [23] and Leonard [24].) Other choices of f have been suggested by Hald [14] and Beale and Majda [15], to provide better representation for the initial vorticity field and produce higher spatial accuracy at later times. This improvement was indicated in the inviscid flow calculations of Nakamura *et al.* [17], Perlman [25], and Beale and Majda [26].

The motion of vortex blobs is governed by a set of ordinary differential equations in the form of Eq. (15) with K replaced by K_δ.

$$\frac{d\boldsymbol{\chi}_j}{dt} = \sum_{\substack{i=1 \\ i \neq j}}^{N} \Gamma_i \mathbf{K}_\delta(\boldsymbol{\chi}_j - \boldsymbol{\chi}_i), \qquad j = 1, 2, \ldots, N. \tag{23}$$

In viscous flow calculations, the number of vortex elements N changes with time due to the generation of vorticity by the action of the no-slip condition along solid boundaries or the Kutta condition at points of separation. This part will be discussed in Section II.4

II.2 *Diffusion*

The transport of vorticity due to diffusion is expressed by Eq. (8). In the random vortex method, the effect of diffusion is implemented by the dispersion of a finite number of vortex elements with finite and constant vorticity according to a 2-dimensional Gaussian statistics. This is based on the fact that the Green function of the 1-dimensional form of Eq. (8):

$$\mathrm{Gr}(y, t) = \sqrt{R/4\pi t} \exp\left(-\frac{R}{4t} y^2 \right) \tag{24}$$

is identical to the probability density function of a Gaussian random variable η with a zero mean and a standard deviation σ:

$$P(\eta; t) = \sqrt{1/2\pi\sigma^2} \exp\left(-\frac{1}{2\sigma^2} \eta^2 \right) \tag{25}$$

if $\sigma = \sqrt{2t/R}$. To construct an algorithm based on this observation, the vorticity field at $t = 0$ is discretized among N particles placed at $y = 0$, each carrying circulation Γ_0/N, where Γ_0 is the initial total circulation at $y = 0$. At later times, the distribution of $\omega(y)$ is approximated by the same number of particles N located at η_i, $i = 1, 2, ..., N$, where $\{\eta\}$ is chosen from a Gaussian population with zero mean and standard deviation σ. If the solution is required at each time step Δt, the particles are displaced every time step using a new set $\{\eta\}$, each having a standard deviation $\sigma = \sqrt{2\Delta t/R}$ (exploiting the linearity of the diffusion equation). For an arbitrary initial condition $\omega(y)$, particles are distributed over the space at $t = 0$ such that at each point $N = N(y) = \Gamma(y)/\Gamma_m$, Γ_m is the maximum circulation assigned to an individual particle.

In two dimensions, the Green function of Eq. (8) is given by

$$\mathrm{Gr}'(x, y, t) = \frac{R}{4\pi t} \exp\left(-\frac{R}{4t} (x^2 + y^2) \right) \tag{26}$$

which is equivalent to

$$\mathrm{Gr}'(x, y, t) = \mathrm{Gr}(x, t)\, \mathrm{Gr}(y, t) \tag{27}$$

where $\mathrm{Gr}(x, t)$ and $\mathrm{Gr}(y, t)$ have the same form as in Eq. (24). The corresponding probability density function is the product of two 1-dimensional probability density functions;

$$P'(n_x, n_y; t) = P_1(n_x; t)\, P_2(n_y; t) \tag{28}$$

P_1, P_2 are given by Eq. (25). Thus, the solution of Eq. (8) is simulated stochastically by a 2-dimensional displacement of the vortex elements in two perpendicular directions using two sets of independent Gaussian random numbers, each having a zero mean and a standard deviation $\sigma = \sqrt{2\Delta t/R}$.

The random walk algorithm is compatible with vortex schemes because of its Lagrangian grid-free form. It can also be applied in regions of large gradients near solid boundaries to move vortex elements which are generated to satisfy the no-slip condition without loss of resolution since it does not depend on the resolution of a grid. Ghoniem and Sherman [18] discuss in detail the stochastic solutions of the diffusion equation with different boundary conditions, its application to the reaction-diffusion equation, and to the combined heat and momentum diffusion that arises in natural convection.

In the random vortex method, the diffusive transport of vortex elements is simulated stochastically by adding to their convective motion an extra displacement drawn from a Gaussian population with a zero mean and a standard deviation σ. The total transport of vortex elements is obtained by adding the two fractional displacements:

$$\chi_j(\chi_j, t+\Delta t) = \chi_j(\chi_j, t) + \sum_k \mathbf{u}(\chi_{jk})\,\Delta t + \boldsymbol{\eta}_j \tag{29}$$

where $\sum_k$ is a kth-order time integration scheme and $\boldsymbol{\eta}_j = (\eta_x, \eta_y)_j$ is a 2-dimensional Gaussian random number, while $\mathbf{u} = \mathbf{u}_\delta + \mathbf{u}_p$ is the total velocity field due to the vortex elements and the satisfaction of the potential boundary condition. The computation of the latter is now presented.

II.3 *Potential Boundary Condition*

The potential boundary condition, the first component of Eq. (3-a), is imposed in the direction normal to the boundaries. The total velocity produced by a vorticity distribution in a semi-confined space can be decomposed into two components,

$$\mathbf{u} = \mathbf{u}_\delta + \mathbf{u}_p \tag{30}$$

where $\mathbf{u}_\delta$ is the field induced by the vorticity within the domain D, given by Eq. (19), while $\mathbf{u}_p$ is an irrotational component added to satisfy the boundary conditions $\mathbf{u}\cdot\mathbf{n} = 0$, where $\mathbf{n}$ is the normal to solid walls (this component can be regarded as a result of image vortices which are located outside the domain.) Since $\mathbf{u}_p$ is irrotational, it can be represented in terms of a potential ϕ where $\mathbf{u}_p = \nabla\phi$ and ϕ is governed by

$$\Delta\phi = 0. \tag{31}$$

ϕ is uniquely determined if its value, its normal derivative or a combination of both is specified on a closed contour (in the second case, ϕ is determined up to an arbitrary constant). On a solid wall,

$$\nabla\phi\cdot\mathbf{n} = -\mathbf{u}_\delta\cdot\mathbf{n}. \tag{32}$$

One way to solve the potential flow problem, formed of Eqs. (31) and (32), is

conformal mapping. This method produces an analytical solution for the potential flow by defining the image system of the vortex elements, provided that the geometry is simple. The solution is grid-free and can provide high resolution close to the boundaries and at points of separation, where it is essential to determine accurately the flux of vorticity into the interior of the domain. For a given distribution of N vortex elements in the physical z-plane, where $z = x + iy$ and $i = \sqrt{-1}$, the total velocity at the center of the jth element is

$$w(z_j) = \left\{ \sum_{\substack{i=1 \\ i \neq j}}^{N} \frac{-i\Gamma_i}{2\pi} \frac{1}{\Delta\zeta} \kappa\left(\frac{|\Delta\zeta|}{\delta_i}\right) + \sum_{i=1}^{N} \frac{i\Gamma_i}{2\pi} \frac{1}{\Delta\tilde{\zeta}} \kappa\left(\frac{|\Delta\tilde{\zeta}|}{\delta_i}\right) \right\} F(\zeta_j) - \frac{i\Gamma_j}{4\pi}\left(\frac{dF}{d\zeta}\right)_j \quad (33)$$

where $w = u - iv$ is the complex velocity, ζ is the complex coordinate in the transform plane, $\Delta\zeta = \zeta_j - \zeta_i$, $\Delta\tilde{\zeta} = \zeta_j - \tilde{\zeta}_i$, and $\tilde{\zeta}$ is the complex conjugate, $\delta_i = \delta F(\zeta_i)$. $F = d\zeta/dz$ is the transformation function that maps the physical z-plane to the upper half of the ζ-plane. The incoming flow is represented by a source of strength $2(H_2 - H_s)$, located at $\zeta = (0, 0)$ in the transform plane, corresponding to $x = -\infty$ in the physical plane. A top-hat profile is obtained at sections one-step-height, or larger, to the left of the step.

For the geometry considered here, shown schematically in Fig. 1, the transformation function can be constructed by applying the Schwarz–Christoffel theorem;

$$F(\zeta) = \frac{d\zeta}{dz} = \pi\zeta\sqrt{(\zeta - \alpha^2)/(\zeta - 1)} \quad (34)$$

where z in this expression is normalized with respect to the channel height H_2, and $\alpha = H_2/H_1$ is the expansion ratio in the channel. $z = z(\zeta)$ is obtained by integrating Eq. (34), which yields

$$z = \frac{1}{\pi}\left(\ln\left(\frac{1+\tau}{1-\tau}\right) - \frac{1}{\alpha}\ln\left(\frac{\alpha+\tau}{\alpha-\tau}\right)\right) \quad (35)$$

where

$$\tau = \sqrt{(\alpha^2 - \zeta)/(1 - \zeta)}.$$

The inverse, $\zeta = \zeta(z)$, require a numerical solution of Eq. (35) by iteration, or a numerical integration of Eq. (34).

II.4 *No-slip Boundary Condition*

In a real flow, the velocity of the fluid at solid boundaries must remain the same as the velocity of the boundary. Any slip velocity is annihilated and vorticity is produced. If the slip velocity is $\mathbf{u}_s$, the total circulation produced to satisfy the no-slip condition is

$$\Gamma = -\int \mathbf{u}_s \cdot d\mathbf{s} \quad (36)$$

where s is the tangential direction to the wall. This scheme of vorticity generation, discussed in more detail by Lighthill [27], was used by Payne [28] to construct a numerical solution for the Navier–Stokes equations around a circular cylinder using a velocity–vorticity formulation on a grid.

Chorin [5] implemented Eq. (36) in the random vortex method to satisfy the viscous boundary condition. The vorticity generated along the wall is discretized into elements separated by a distance S. To improve the resolution, the element at each point is subdivided into several elements such that $\Gamma < \Gamma_m$, where Γ_m is the maximum allowable vortex strength. These elements leave the wall by diffusion, to become part of the interior vorticity field at later times.

At moderate and high values of the Reynolds number, and within a thin wall sublayer Δ_s, the velocity component normal to the wall is very small compared to the component parallel to the wall. Moreover, variations in the velocities in the direction parallel to the wall are smaller than the variations in the direction normal to it. This simplifies the expression of the vorticity and its transport equation. In principle, these observations are valid only for boundary-layer flow at high Reynolds numbers. If Δ_s is restricted to $O(\sqrt{\Delta t/R})$, i.e., the temporal growth of the boundary layer during few time steps, these properties can be used even if the interior flow is not a boundary-layer flow. In the following, we employ the results of boundary-layer scaling to reform the shape of the vortex elements near the boundaries and insure high resolution in the direction normal to the wall. This also leads to saving in the computations.

In this section, the coordinate system (x,y) is used to represent the parallel and the normal to the wall, respectively. Geometric coordinate transformation is employed whenever necessary for adapting the algorithm to match the coordinates of the channel to the coordinates of various walls. Inside the wall sublayer, $\partial v/\partial x \ll \partial u/\partial y$, and the expression of the vorticity is reduced to

$$\omega = -\partial u/\partial y \tag{37}$$

Accordingly, the vorticity distribution can be approximated by a number of sheets, of finite length S, that remain parallel to the wall while they transport velocity jumps δu normal to the wall. If the circulation per unit length carried by a sheet is $\gamma_i = (\delta u)_i = \Gamma_i/S$, then for a number of sheets M, the vorticity distribution is given by

$$\omega(\boldsymbol{\chi}) = \sum_{i=1}^{M} \gamma_i f_\Delta(\mathbf{x} - \boldsymbol{\chi}_i) \tag{38}$$

where f_Δ is the vortex sheet core function, defined as

$$f_\Delta(\mathbf{x}) = \frac{1}{S}\delta(y)\left\{H\left(x+\frac{S}{2}\right) - H\left(x-\frac{S}{2}\right)\right\} \tag{39}$$

and the $\delta(\ )$ is the Dirac delta function, while $H(\ )$ is the Heavyside function. The

corresponding velocity distribution is obtained by substituting Eq. (38) into Eq. (37) and integrating:

$$u(\mathbf{x}) = \sum_{i=1}^{M} \gamma_i \mathbf{K}_{\Delta}(\mathbf{x} - \boldsymbol{\chi}_i) \tag{40}$$

where

$$\mathbf{K}_{\Delta}(\mathbf{x}) = H(y)\left\{H\left(x + \frac{S}{2}\right) - H\left(x - \frac{S}{2}\right)\right\}. \tag{41}$$

To compute the velocity of a vortex sheet; the velocity at a point is averaged over the length of the sheets,

$$u(\boldsymbol{\chi}_j) = \frac{1}{S}\int_{x_j - S/2}^{x_j + S/2} u(x', y)\, dx'.$$

Substituting from Eq. (40) and integrating,

$$u(\boldsymbol{\chi}_j) = \sum_{i=1}^{M} \gamma_i D_{ij} H(y_j - y_i) \tag{42}$$

where

$$D_{ij} = \frac{1}{S}\{(x_j - x_i + S) H(x_j - x_i + S) - 2(x_j - x_i) H(x_j - x_i) + (x_j - x_i - S) H(x_j - x_i - S)\}. \tag{43}$$

By inspection, we find that $D_{ij} = 0$ if $|x_j - x_i| > S$, i.e., if the two sheets do not overlap in the x- direction. Otherwise, the contribution is proportional to the overlap. Thus,

$$\begin{aligned} D_{ij} &= 1 - \frac{|x_i - x_j|}{S} \qquad \text{if} \quad |x_j - x_i| < S, \\ &= 0 \qquad\qquad\qquad\quad \text{if} \quad |x_j - x_i| > S. \end{aligned} \tag{44}$$

Since the u- velocity is obtained by averaging along a length S, the accuracy of the algorithm is expected to be $O(S^n)$, while n depends on the degree of overlap between the sheets. The v- component is computed by integrating the continuity equation;

$$v(\mathbf{x}) = -\frac{\partial}{\partial x}\int_0^y u\, dy' \tag{45}$$

and using Eq. (42) for the u- velocity. The integral I yields

$$I = \sum_{i=1}^{M} \gamma_i D_{ij}(y_j - y_i) H(y_j - y_i) \tag{46}$$

thus, for the sheet at χ_j, Eqs. (45) and (46) yield

$$v(\chi_j) = -\left(\frac{I^+ - I^-}{S}\right) \tag{47}$$

where $I^{\pm}$ are evaluated at $(x_j \pm S/2, y_j)$.

Vortex sheets diffuse perpendicular to the wall only, according to the boundary layer argument presented before. Thus, if $\chi_j(\chi_j, t)$ is the center of a vortex sheet, its variation with time is given by

$$\chi_j(\mathbf{X}_j, t + \Delta t) = \chi_j(\mathbf{X}_j, t) + \mathbf{u}(\chi_j)\,\Delta t + (0, \eta)_j. \tag{48}$$

The two components of $\mathbf{u}(\chi_j)$ are given by Eqs. (42) and (47).

II.5. *Downstream Boundary Condition*

The numerical scheme described in this section is used to compute the flow field in a channel with a rearward-facing step, Fig. 1. At time $t = 0$, the initial conditions consist of a potential flow produced by a source located at $x = -\infty$, and a vortex sheet along the walls. The strength of the vortex sheet is calculated using Eq. (36), where u_s is the slip velocity generated by the potential flow. Although the scheme is time- dependent, our interest here is confined to the steady-state solution.

The computational domain is $X_{\min} \leqq x \leqq X_{\max}$. At the inlet section, $x = X_{\min}$, the velocity profile is uniform provided that $|X_{\min}| \geqq H_s$. This is the velocity produced by the potential component of the flow. The growth of the boundary layers along the two walls of the entry channel before the step does not affect the velocity at the inlet section because of the symmetry of the vorticity distribution.

At $x = X_{\max}$, an exit boundary condition is imposed. At this section, all the vorticity is deleted. In the computation, $X_{\max}$ was chosen to be larger than the reatachment length, X_r, to minimize the effect of the downstream boundary conditions on the developing flow near the step. This choice will be discussed in more detail later.

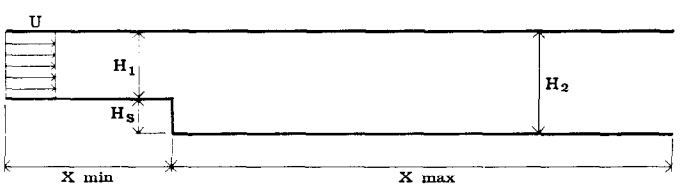

FIG. 1. The geometry of the computational domain.

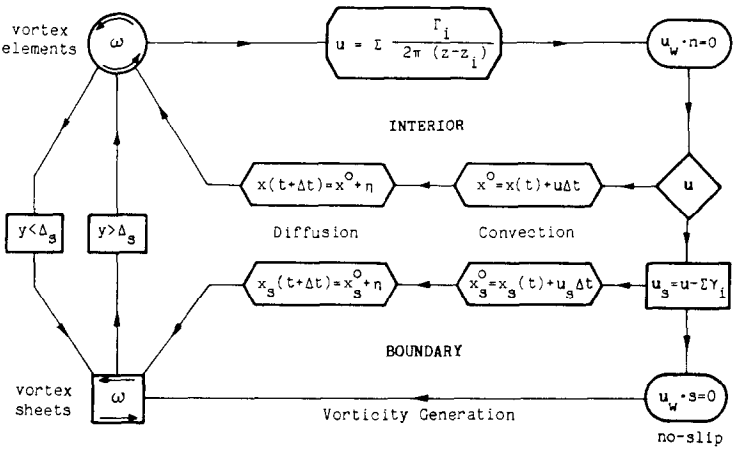

FIG. 2. Schematic diagram showing the structure of the algorithm for the random vortex method.

II.6 *Algorithm*

The vortex algorithm is described schematically in Fig. 2. By extending the application of Eq. (40) to the wall, $y=0$, the slip velocity $\mathbf{u}_s$ is computed and the strength of the new vortex sheets is evaluated according to Eq. (36). If $|\Gamma| > \Gamma_m$, where Γ_m is the maximum circulation of a sheet, several sheets are used to carry the total vorticity into the field. If $|\Gamma| < \Gamma_m$, nothing is done. This provides a mechanism that can be used to refine the resolution of the computation, without increasing unjudiciously the number of vortex elements.

Vortex sheets associated with each wall are displaced according to Eq. (48). If $y_j > \Delta_s$, the sheet is transformed into a vortex blob with $\Gamma_j = S\gamma_j$. Sheets that are transported outside the physical domain are reflected back across the wall. Since a vortex sheet and a vortex blob are two different representations of the same object, they should produce the same velocity field between their centers and the wall. This is accomplished by the following choice for the core radius:

$$\delta = S/\pi \tag{49}$$

provided that $\Delta_s < \delta$; which is always satisfied in the computations.

The velocity field in the interior is computed using Eq. (33) and the vortex blobs are transported according to Eq. (29). Vortex blobs that fall within any of the wall sublayers are transformed into vortex sheets with $\gamma_j = \Gamma_j/S$. If a blob jumps outside the computational domain, an unlikely event if $\Delta_s > 2\sigma$, it is deleted. Care must be exercised in transforming back and forth from the channel coordinates for vortex blobs to wall coordinates for vortex sheets.

III. Solution

The numerical scheme described in the previous section is now applied to compute the steady flow field in the channel in Fig. 1 at moderate Reynolds numbers. This flow can be regarded as an entry flow in a channel with two parallel walls, followed by a confined recirculating flow behind a rearward-facing step. Results are used to study the accuracy and convergence of the numerical algorithm and the properties of the recirculating flow. The channel flow is stable and possesses a well-established analytical solution. The recirculating flow is unstable beyond low Reynolds numbers, and its structure is complicated by the interactions between a developing boundary layer on the top wall, a separating shear layer at the step, a recirculation zone and a developing boundary layer after reattachment on the bottom wall. It is, thus, a challenging test for the accuracy and robustness of a numerical scheme.

The range of Reynolds numbers, based on the step heigth H_s and the uniform velocity U at the inlet section, is limited to $70 < R < 230$. Within this range, Denham and Patrick [29], which we will refer to as D&P, and Armaly *et al.* [30]

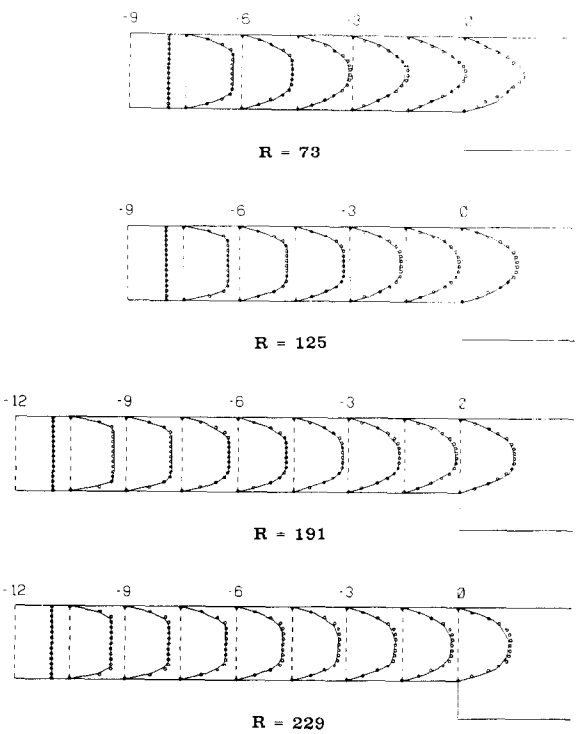

FIG. 3. Sreamwise velocity profiles at different Reynolds number for a developing flow in a channel with parallel walls, before the step. The computed solutions are represented by solid lines and the analytical solutions are shown by open circles.

have shown experimentally that the recirculating flow remains 2-dimensional up to $R = 229$. Near the upper limit, weak 3-dimensional structures and spanwise variation in the velocity were observed around the reattachement point. The application of a 2-dimensional flow model is, hence, physically justifiable below this

numerical parameters until no further changes occured.

Figure 3 shows a comparison between the computed solutions, depicted by solid lines, and the analytical solutions, represented by open circles, for an entry flow in a channel with parallel walls, upstream of the step. Results are obtained by averaging the solution over 50 time steps to remove the effect of the statistical error, starting 150 time steps after $t = 0$. The presence of the step at the end of the channel does not induce any measurable effect since the developing flow is of the boundary-layer type, i.e., it may be approximately described by parabolic equations. The inlet velocity profile is a plug flow at $x = X_{\min}$. The analytical solution is constructed by matching the solution of two developing boundary layers on both walls with an

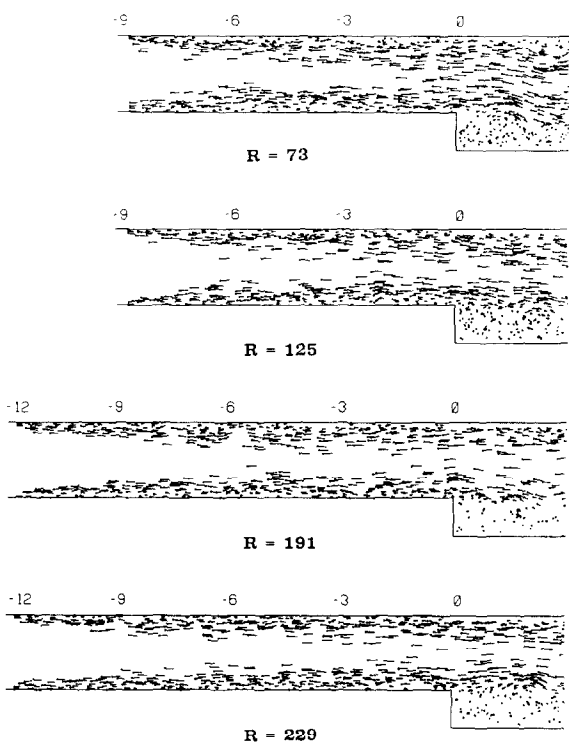

FIG. 4. Instantaneous vorticity fields for the flows of Fig. 3. The solid circle depicts the location of a vortex element and the line is its velocity vector.

accelerating flow in the interior (Schlichting [31] and Van Dyke [32]). All numerical solutions were obtained using the following set of parameters: $S = 0.5$, $\Gamma_m = 0.0417$, $\Delta t = 0.3$ with a second-order time-integration scheme in Eq. (29) while $\Delta_s = 2\sigma$. The accuracy of the numerical scheme is evident from the results.

Figure 4 shows instantaneous vorticity fields for the flows in Fig. 3. They are presented in terms of all the vortex blobs used in the interior, each element shown by a solid circle and a line depicting its instantaneous velocity vector. All vortex elements carry the same value of the circulation Γ_m. Vortex sheets on the walls are not shown in the figure due to their high concentration. These figures exhibit the self-adaptive nature of the computations that was mentioned earlier. Vortex elements are found only within the boundary layers, and the thickness of these layers is controlled by the Reynolds number. The potential core, where the velocity is uniform, is void of vortex elements. The merging of the two boundary layers developing on the opposite walls can be observed, while the potential core is diminishing faster as the Reynolds number is reduced.

Figure 5 shows the effect of the number of time steps used to produce the average velocity profiles. The statistical error associated with the random walk simulation of diffusion is averaged out using as low as 10 time steps. Instantaneous velocity profiles are slightly more rugged than those obtained by averaging over 10 steps. However, these local pertubations decay since this flow is stable and steady, and increasing the sample does not change the average results.

Figure 6 depicts a comparison between the computed solutions of the average streamwise velocity profiles for the recirculating flow and the experimental results of

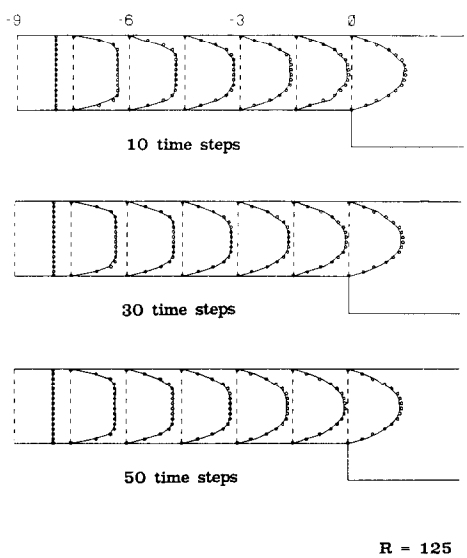

FIG. 5. Effect of avaraging on the accuracy of the computed solution for a developing flow between parallel walls at $R = 125$.

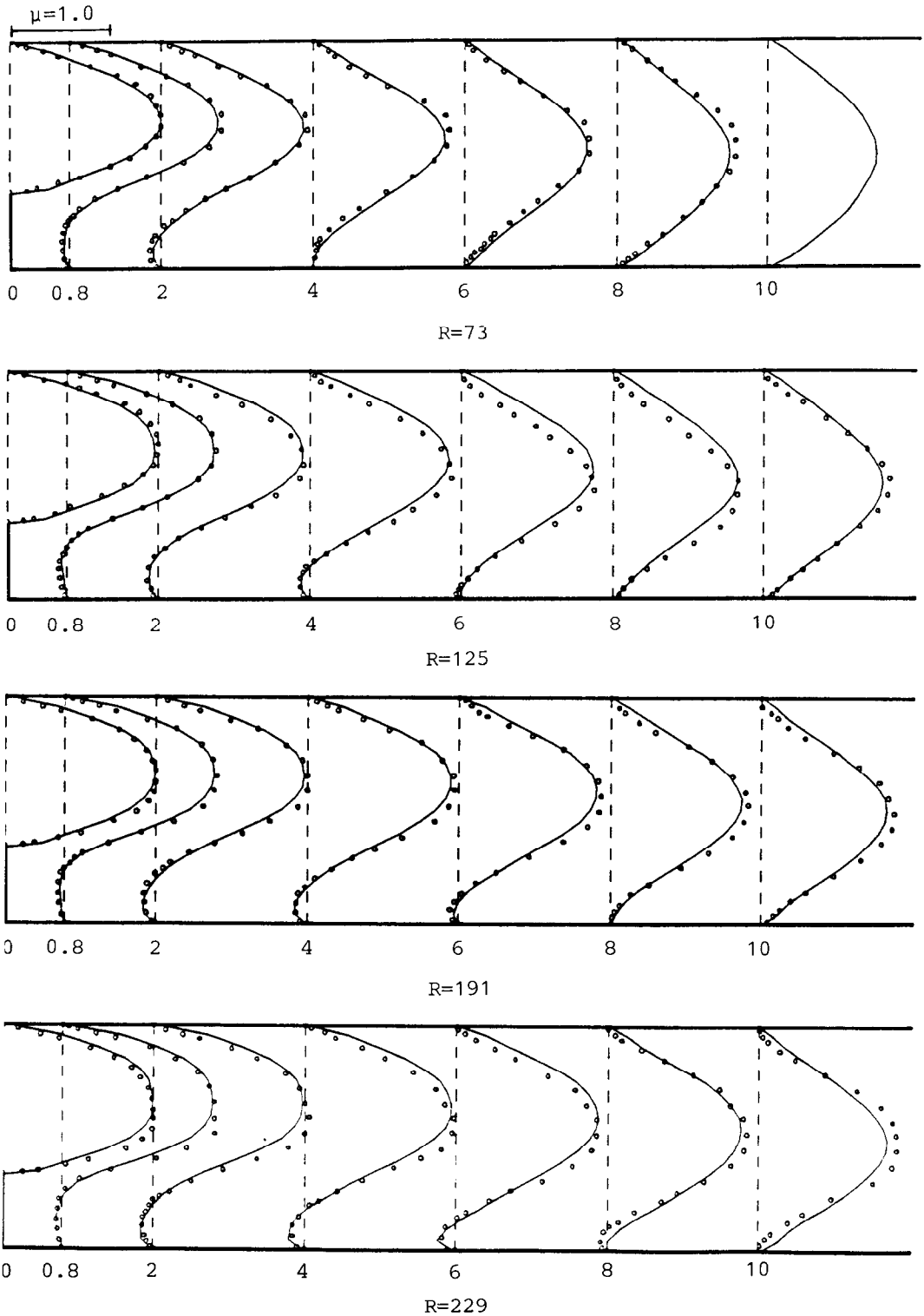

FIG. 6. Comparison between computed and measured average streamwise velocity profiles at different Reynolds number for a recirculating flow behind a rearward-facing step. The continuous line is for the numerical solution and the open circles are the experimental results of Denham and Patrick. Dimensions are normalized with respect to step heights, and $R = UH_s/v$.

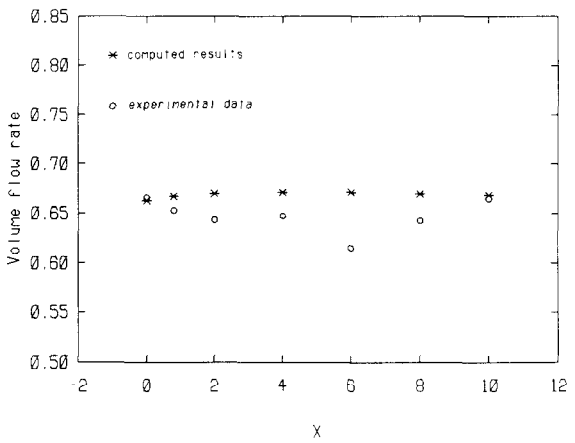

FIG. 7. Volume flow rate at different sections downstream of the step at $R = 125$: * for the computed results and 0 for experimental data.

D&P at different Reynolds numbers. The same set of numerical parameters employed to produce Fig. 3 was used to obtain these results. In actual computations, both fields were obtained in the same run. The value of $X_{\min}$, at which the inlet condition of a plug flow was applied, was varied until the computed velocity profile at the step approached the corresponding experimental velocity profile. Averaging started when the total circulation $\Gamma_t = \sum|\Gamma_i|$, where the summation is performed over all vortex elements, reached a constant value (see Fig. 18). The numerical solution reached steady state when no further significant changes were observed on the average velocity profiles. At this point, the streamlines constructed using these average velocity profiles formed closed loops around a common center.

The numerical solutions show very good agreement with the experimental results except for two cases: (1) the range of $4 \leqslant x \leqslant 8$ at $R = 125$, and (2) around the reattachment point at $R = 229$, where noticeable deviation is detected. In the first case, the experimental results did not satisfy continuity, expressed as $\int u(x, y') = \text{constant}$, at $x = 4$, 6, and 8, as shown in Fig. 7. The deviation is thus attributed to inaccuracy in the experimental measurements. For the second case, D&P confirmed the existence of secondary 3-dimensional flow around the zone of reattachment at $R = 229$. Results of Armaly *et al.* [30] show the onset of 3-dimensional motion around the same value of R.

A sample of the corresponding instantaneous vorticity fields are shown in Fig. 8. Close examination of the figure reveals that the vorticity field is composed of a small number of large eddies, while each of the latter is formed of a large number of computational vortex elements. The flow field is formed of four regions that merge as the flow develops: a boundary layer growing on the top wall, a boundary layer forming on the step wall and separating at the step, a separating shear layer and a

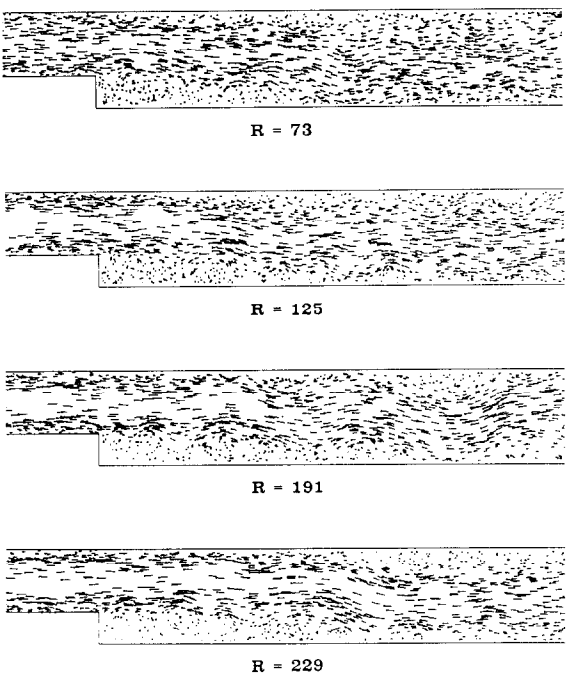

FIG. 8. Instantaneous vorticity field for the flows in Fig. 6.

recirculation zone downstream the step, and a boundary layer that develops on the bottom wall after the recirculation ends and the flow is reattached to the wall.

Figure 9 shows the cross-stream velocity component. The streamline plots for the mean flows are shown in Fig. 10. These plots were constructed from particle paths generated using the average velocity data computed on a uniform grid. The initial positions of the particles were distributed arbitrarily in the channel to obtain higher resolution, hence, the plots do not conform with the conventional equipartitioned stream function plots.

The variation of the reattachment length, X_r, with Reynolds number is summarized in Fig. 11. The reattachment point is defined as the point on the bottom wall where the velocity gradient $\partial u/\partial y = 0$, or the point at which the separating streamline intersects with the bottom wall. Using either definition, the value of X_r can vary within $\pm H_s/2$, depending on the accuracy of the plots for the average velocity profiles or the streamline contours. The first definition was used to plot Fig. 11. While X_r can be used as an integral measure for the accuracy of the numerical results, the detailed velocity profile plots in Fig. 6 remains as the decisive test.

The effect of the velocity profile at the step on the flow field was investigated by varying $X_{\min}$, thus allowing the boundary layer in the developing flow to grow

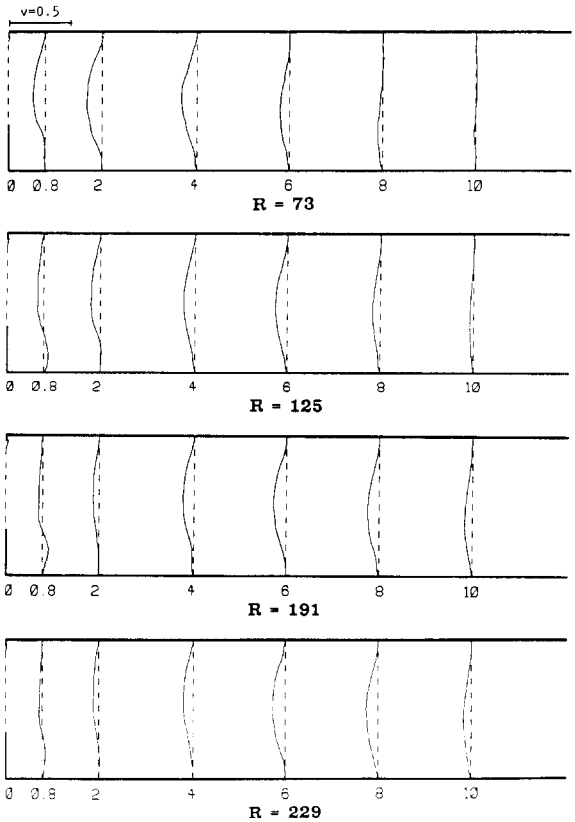

FIG. 9. Average cross-stream velocity profiles corresponding to the flows in Fig. 6.

further and the flow at the step to approach the experimental profile. Results are shown in Fig. 12, compared with the experimental velocity profiles of a flow with a nearly fully- developed velocity profile at the step at $R = 191$. As expected, the reattachment length increases as the boundary layer thickness increases at the step.

The average pressure distribution for $R = 191$, presented in Fig. 13 in the form of a 3-dimensional plot, was obtained using a finite difference solution of Eq. (6) and the average velocity distribution obtained from the vortex simulations. Details of the solution scheme are presented elsewhere (Cagnon [33]). The scaling suggested by Westphal *et al.* [34] for a turbulent recirculating flow was used to present the results for the pressure along the bottom wall in Fig. 14. The similarity between the pressure coefficient at different Reynolds numbers, when plotted against a downstream coordinate normalized with respect to the recirculation length, is approximately satisfied only within the recirculation zone. After reattachment, the pressure gradient is a strong function of the Reynolds number.

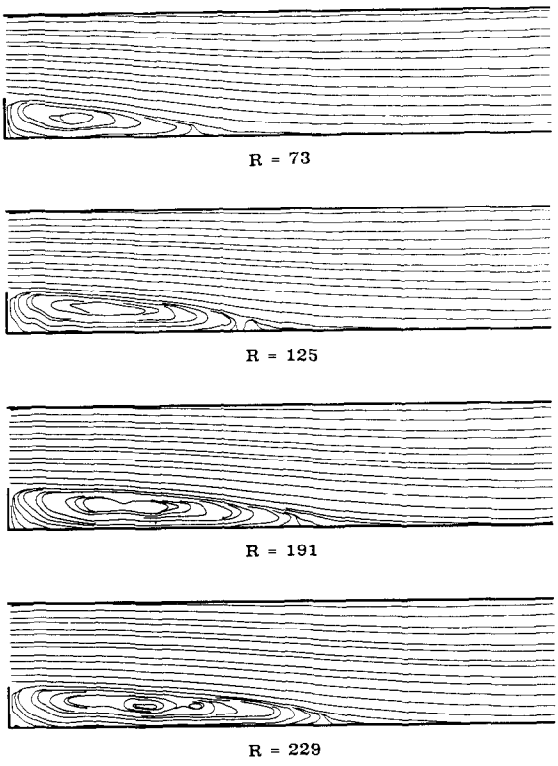

FIG. 10. Average streamline plots for the flows of Fig. 6.

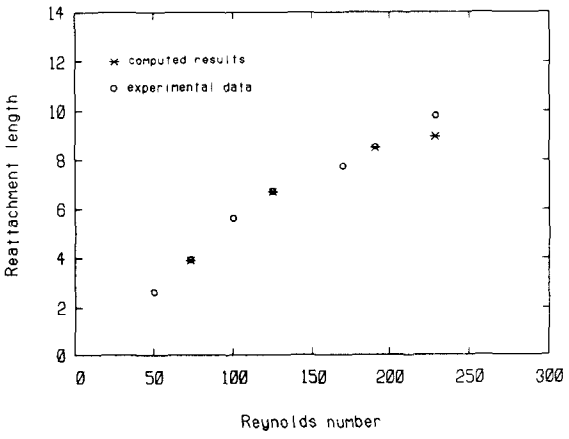

FIG. 11. Comparison between the numerical and experimental reattachment length X_r, normalized with respect to the step heights, with Reynolds number (X_r vs R).

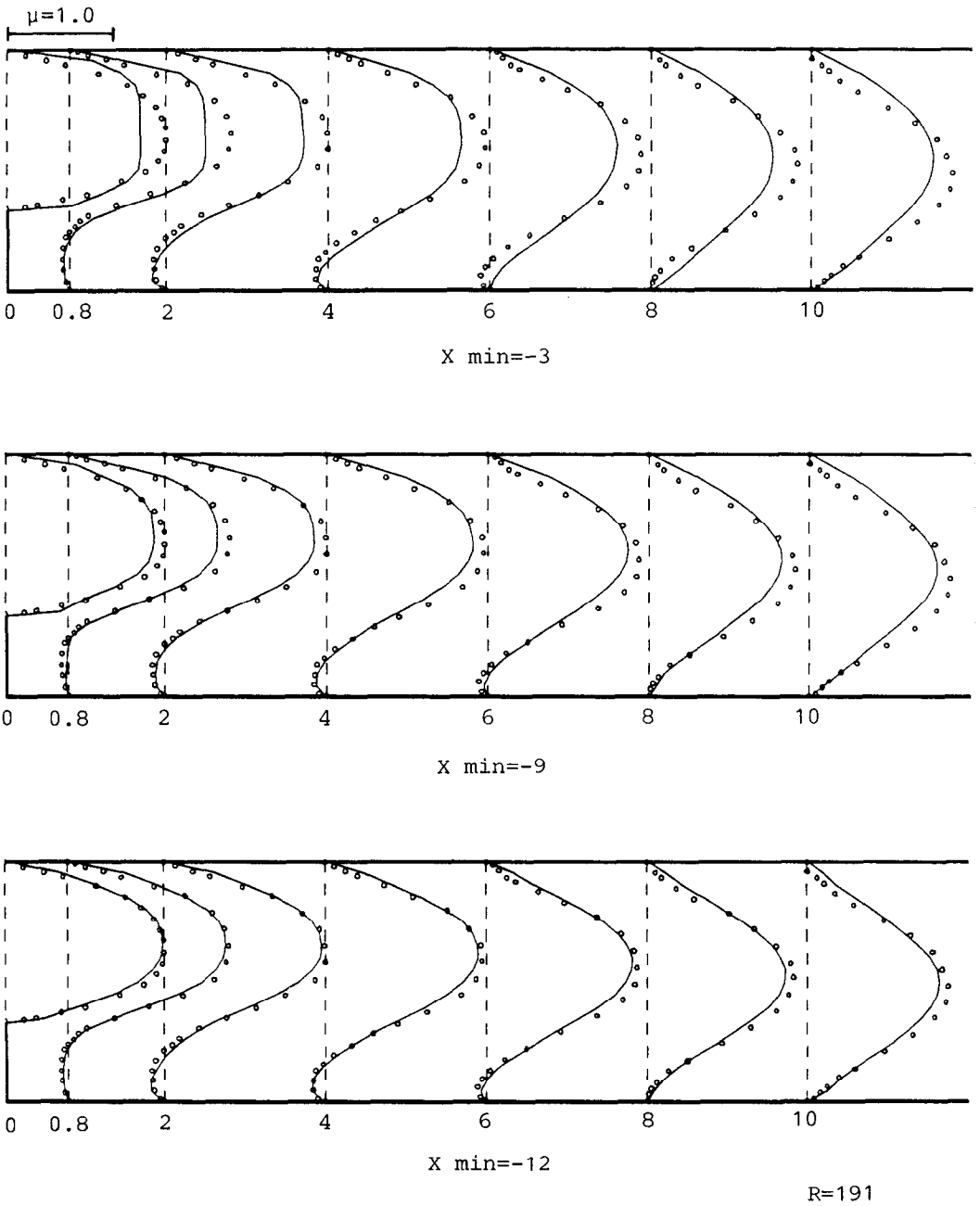

FIG. 12. Average streamwise velocity profiles for a flow at $R = 191$ with different velocity profiles at the step. The continuous lines are for the numerical simulation and the open circles represent the experimental velocity profile. X_{min} refers to the length of the computational domain upstream of the step.

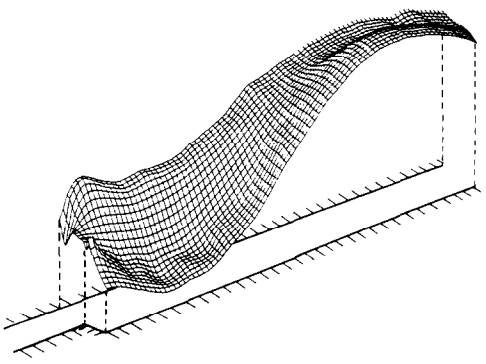

FIG. 13. Pressure distribution for a flow at $R = 191$.

IV. DISCUSSION

In this section, we discuss the accuracy of the random vortex method using the results of numerical examples. In the process, sources of errors are identified and a scheme to optimize the choice of the numerical parameters is suggested. The numerical parameters used in the discretization of the equations are: (1) the length of a vortex sheet S; (2) the circulation of a vortex element; a sheet or a blob, Γ_m; (3) the thickness of the wall sublayer Δ_s; and (4) the time step Δt. One more parameter that affects the calculation is $X_{\max}$, the length of the computational domain downstream the step. At this section, vortex elements are deleted; their effect being considered very small on the upstream flow. It was found that

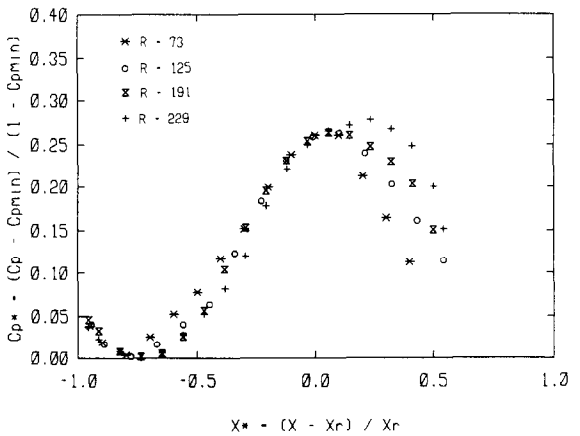

FIG. 14. Normalized pressure coefficient vs the normalized downstream distance from the step for four values of Reynolds number.

$X_{max} \sim 2X_r$ is a reasonable choice, smaller values of X_{max} produce shorter recirculation length and longer values do not change X_r.

To investigate the effect of each parameter on the accuracy of the results, a set of numerical experiments was conducted in which only one parameter was varied, while the other parameters were maintained at a fixed small value. A comparison between the computed and the measured velocity profiles were used to assess the accuracy. In most cases, the effect was most strongly felt around the section where reattachment occurs, while the rest of the profiles remained essentially the same. Thus, the reattachment length was used as an integral measure for the accuracy.

To examine the effect of Γ_m, we used the following set of parameters: $S = 0.5$, $\Delta_s = 2\sigma$, $\Delta t = 0.3$, and a second-order time integration scheme for Eq. (29), while $X_{max} = 15$ for $R = 73$–191. For $R = 73$, X_{max} was varied between 12 and 15 without producing any noticeable effect on the computed velocity profiles. For $R = 229$, we used $X_{max} = 15$ and 21, since X_r is expected to be around 10. The computed value of X_r increased from 8.5 to 9 with increasing X_{max}. In the following, the effect of Γ_m on the accuracy of the computations is described.

At a particular value of R; and for a fixed value of S, the total number of vortex elements needed to saturate the field should be inversely proportional to Γ_m, since at steady state $N = \int |\omega| \, dA/\Gamma_m$, where $|\omega|$ is the steady-state vorticity distribution. However, computational results showed that this relationship is satisfied only for $\Gamma_m \leqslant \Gamma^*$. At larger values of Γ_m, the reattachment length is small, $X_r \sim 4$, and the computed velocity profiles are almost independent of R. At that level, N is found to be independent of Γ_m, and the vorticity field is contaminated with parasite vortex elements generated due to the inaccurate discretization of the vorticity field.

The total number of vortex elements N increases as Γ_m is decreased, while X_r becomes longer, as shown in Figs. 15 and 16, respectively, for $R = 191$ and

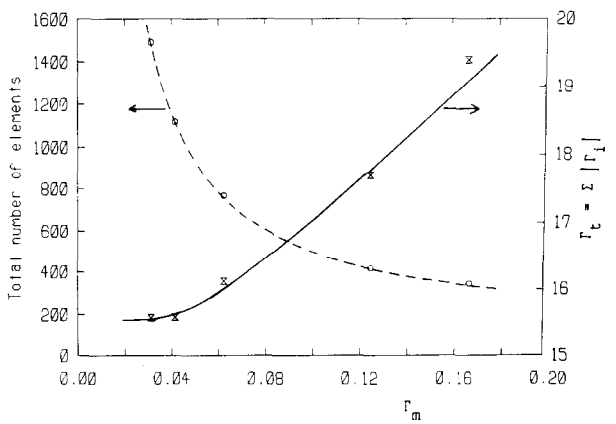

FIG. 15. The effect of the circulation of vortex elements on the total number of elements used to discretize the vorticity field and the total absolute circulation for $R = 191$ and $X_{min} = -1.0$.

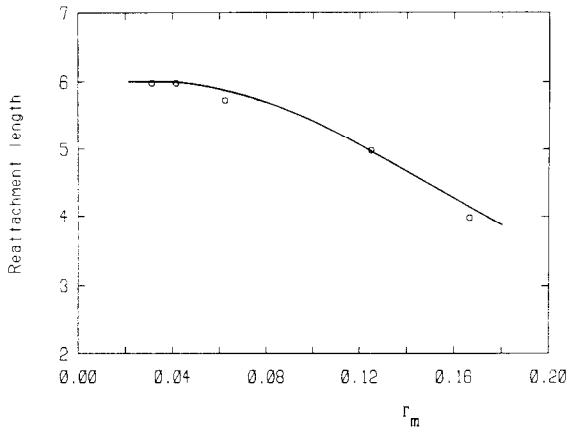

FIG. 16. The effect of the circulation of vortex elements on the reattachment length for the case $R = 191$ and $X_{\min} = -1.0$.

$X_{\min} = -1.0$. Meanwhile, the total value of circulation $\Gamma_t = \sum|\Gamma_i|$ decreases, indicating that fewer vortex elements are generated. The latter can be confirmed by inspecting Fig. 17, obtained from computations for $R = 191$ and $X_{\min} = -3.0$, where the vortex blobs used in the computations are plotted according to their sign: a "+" indicating a positive (counterclockwise) vortex, while a "□" is a negative (clockwise) vortex. Both figures show that by reducing Γ_m from 0.0624 to 0.0417, the number of negative blobs inside the top-wall-boundary layer, which is formed of positive vorticity, is decreasing and the accuracy of the simulation is improving. For values of $\Gamma_m < \Gamma^* = 0.0417$, the number of vortex elements generated became proportional to Γ_m so that $\Gamma_t = \sum|\Gamma_i| = \text{constant}$, and X_r became independent of Γ_m.

From the description of the algorithm in Section II, it is clear that the process of vorticity generation is dependent on the velocity field induced by the existing vortex elements. If vortex elements do not discretize the vorticity field accurately, the induced velocity field will be contaminated with large errors. Vortex elements with large values of Γ_m, which should have been divided into a number of vortices with smaller Γ_m when they were generated, produce errors in the velocity field. That, in turn, results in the generation of vortex element of the opposite strenght. These are "error" vortices, or parasite vortex elements that should not have been generated had the initial discretization been accurate. By decreasing Γ_m, the number of parasite vortices is decreased so that the total number of vortex elements N approximately satisfies $N\Gamma_m = \text{const}$.

The algorithm of vorticity generation at the wall represents a "self-healing" mechanism of the vortex algorithm and the above observations can be used to construct a consistency test for the computations. If the value of Γ_m is reduced by a factor β, N should increase by the same factor, otherwise the computations should be repeated with smaller values of Γ_m until this condition is satisfied. Note that the

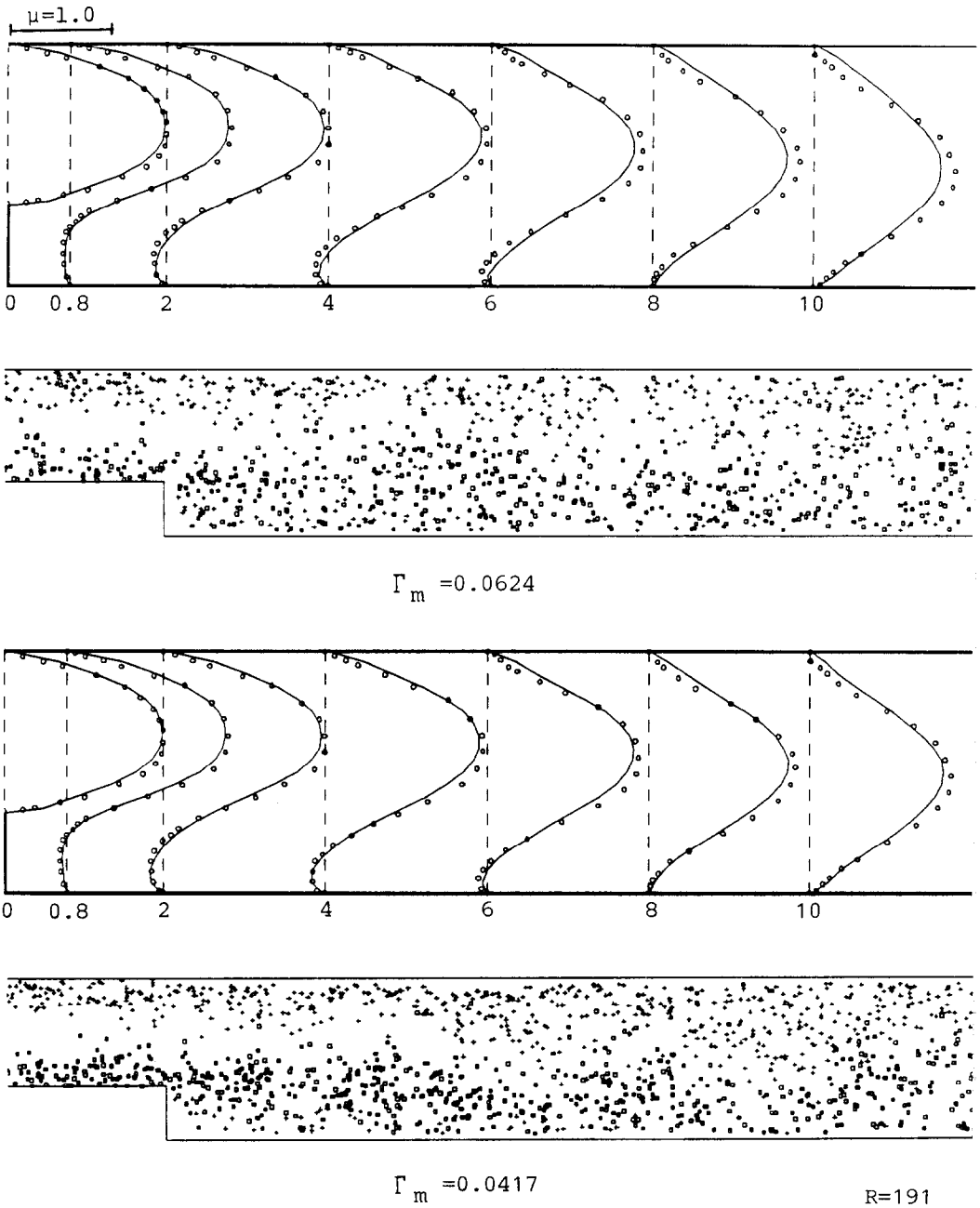

FIG. 17. Average streamwise velocity profiles and instantaneous vorticity fields depicting the sign of circulation of the vortex elements for a flow of $R = 191$, $X_{\min} = -3$, for two different values of circulation. The + sign indicates a positive (counterclockwise) vortex while a □ sign is a negative (clockwise) vortex.

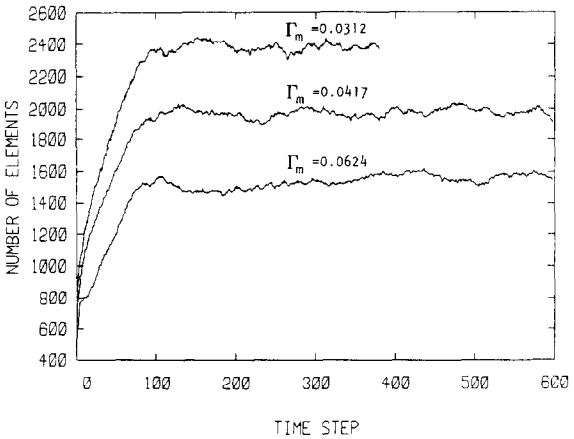

FIG. 18. Variation of the total number of vortex element with time, for the flow at $R = 125$, with $X_{min} = -3.0$.

computations do not have to be carried until the velocity field reaches a stationary state, since the number of vortex (blobs and sheets) reaches a constant value within the first 100 time steps, as shown in Fig. 18 for $R = 125$ and $X_{min} = -3.0$. This condition if sufficient, but not necessary, for accuracy and the presence of a small number of parasite vortices of opposite signs, if their number is small, may suppress their ill effect.

Figure 19 shows the variation of the total number of vortices with Reynolds number (for $R = 229$, N corresponds to $X_{max} = 15$). The figure suggests that, within this range of Reynolds number, the number of elements necessary to achieve a given

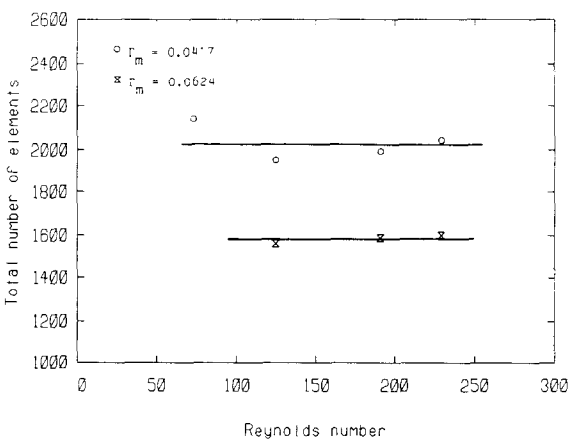

FIG. 19. Total number of vortex elements vs Reynolds number for two different values of vortex element circulation.

accuracy is independent of R. This trend may be related to the fact that within our range of Reynolds number, the dynamics of the flow, which can be characterized as a balance between the effect of inertia and viscous forces, remains almost the same. We did not observe transition, strong self-sustained oscillations, or strong separation along any of the channel walls. The onset of any of these phenomenon would require an increase in the number of computational elements to resolve the associated vorticity field. Increasing the Reynolds number within this range causes the boundary layers to become thinner, and the computational vortex elements to concentrate closer to the walls. It was observed, however, that for the recirculating flow, the number of time steps necessary to reach steady state increased as R increased, ranging approximately from 150–400. It is suspected that weak unsteadiness may be responsible for this phenomena.

To study the effect of the time step on the steady state results, the value of Δt was varied from 0.15 to 0.3, while Γ_m was maintained at the smallest value. The Courant time step corresponding to the sheet length is 0.6, and hence the values used in the computations are small. No noticeable changes were observed in the velocity profiles. Moreover, when $\Gamma_m \leqq \Gamma^*$, employing a first-order time integration scheme did not affect the accuracy of the steady-state solution. However, all the results presented here were obtained with second-order time integration for the motion of vortex blobs in the interior. It should be emphasized that this conclusion applies only to the steady-state solution, and that time-dependent solutions may require special care in the time integration (for results concerning the effect of the time step on a time-dependent flow, see Milinazzo and Saffman [35], Roberts [36], and Sethian and Ghoniem [12].)

No attempt was made to change the value of S, the sheet length, since the results obtained with $S = 0.5$ proved to be accurate. It is conceivable that when the number of vortex elements N is large, a high degree of overlap between the sheets is established within the wall sublayer Δ_s. This overlap reduces the effect of the length of each individual element. It should be noted that if the flow separates and reattaches along a particular wall due to a strong pressure gradient, smaller values of S may be required to resolve the vorticity field. The presence of a separation bubble on a wall causes strong variation of vorticity in the streamwise direction, and S must become small enough to capture this change. This situation was not encountered in the present computations.

The thickness of the wall sublayer was varied from 2σ to 3σ without noticeable effect on either the total number of elements or the velocity profiles. With the first choice, $\Delta_s = 0.1 - 0.18\, H_s$, depending on the Reynolds number, which is equivalent to 0.033–0.06 of the channel height downstream of the step. In a difference approximation, this would correspond to a single grid point away from the wall if 30 points were employed across the channel. In the vortex calculations, three sheets appeared on the average between the wall and the interior. This provided finer resolution for the vorticity field within the wall sublayer. Since the validity of the vortex sheet algorithm is dependent on the boundary layer approximation, which ceases to apply where the main flow direction experiences a sudden change, caution

must be exercised near corners. In this computation, each wall sublayer ended immediately before the intersection between the two sheet zones at the step and around the corner. A vortex sheet leaving either zones at this point is turned into a vortex blob.

In all results presented, the sheet velocity normal to the wall was taken into account. However, when Δ is limited to 2σ, the value of v in Eq. (47) is very small and can be neglected. Numerical experiments produces the same results when v is set to zero in Eq. (48). This represents saving in the programming effort, but not in computational time, since the boundary layer calculation, while more complicated to program, requires much less time than the interior calculations.

V. Conclusions

Computations of a recirculating flow downstream a rearward-facing step in a channel, at values of Reynolds number for which 2-dimensional, steady flow is experimentally observed, were performed using the random vortex method. Our choice of the test cases and the regime of Reynolds number, while mandated by the availability of experimental results for comparison, represent a problem that is fundamentally challenging and practically important. Converged results, obtained by successive stepwise refinement of the numerical parameters, showed good agreement with analytical solutions, or fell within the experimental tolerance. The behaviour of the error suggests that the variation of the number of vortex elements as a function of the circulation of each element can be used to judge the accuracy of the computed solution. The criterion depends on the fact that, within a specified computational domain, the total circulation in the field should be invariant to the strength of a computational vortex element.

The numerical solutions of steady problems show that the number of elements used in the simulation has the strongest influence on the accuracy. Using a small number of elements to discretize the vorticity field produces errors that reduce the reattachment length for the recirculating flow. In this computation, when the number of vortex elements exceeds a critical value, the initial separartion between vortex sheets and the time step, if chosen small enough, is of secondary importance. The number of vortex elements required to achieve accurate results is almost independent of the Reynolds number. Averaging over ten time steps removes the statistical error and yields essentially smooth profiles that compare favorably with the analytical solution of a steady channel flow. For the recirculating flow, as the Reynolds number increases, averaging over an increasing number of time steps is necessary to compute a steady-state solution.

It should be emphasized that the method employed here is time-dependent, and not limited to low Reynolds number. Several open questions regarding the scheme, and the flow, remain to be answered by analysis or more computations: What is the optimum choice of the core function for viscous flow simulations, what is the optimum choice of the numerical parameters under unsteady conditions, how to

reduce the computational time without sacrificing accuracy, whether the flow within this regime is weakly or strongly stable, and how does this stability phenomenon depend on the Reynolds number.

Acknowledgment

This work is supported by the National Science Foundation Grant CPE–8404811 and the Air Force Office of Scientific Research Grant AFOSR84–0356.

References

1. A. J. Chorin and P. Bernard, *J. Comput. Phys.* **13**, 423 (1973).
2. K. Kuwahara and H. Takami, *J. Phys. Soc. Japan* **34**, 247 (1973).
3. P. Saffman and G. Baker, *Ann. Rev. Fluid Mech.* **11**, 95 (1979).
4. R. Krasny, *J. Comput. Phys.* **65**, 292 (1986).
5. A. J. Chorin, *J. Fluid Mech.* **57**, 785 (1973).
6. A. J. Chorin, *J. Comput. Phys.* **27**, 423 (1978).
7. A. J. Chorin, *SIAM J. Sci. Statist. Comput.* **1**, 1 (1980).
8. W. T. Ashurst, presented at the 2nd *Symposium on Turbulent Shear Flows, Imperial College, London, July* 1979.
9. A. F. Ghoniem, A. J. Chorin and A. K. Oppenheim, *Philos. Trans. Roy. Soc. London A* **303**, 303 (1982).
10. C. C. Hsiao, A. F. Ghoniem, A. J. Chorin and A. K. Oppenheim, *in*: *Proceeedings of the 20th Symposium (International) on Combustion, Ann Arbor, Michigan*, 1984, edited by E. Dabora *et al.* (The Combustion Institute, Pittsburg, Pa., 1985), p. 495.
11. A. Y. Cheer, (Rep. PAM–145,) Center for Pure and Applied Mathematics, University of California, Berkeley, April 1983.
12. A. F. Ghoniem and J. A. Sethian, *The AIAA 23rd Aerospace Sciences Meeting, Reno, Nevada, January* 1985, AIAA–85–0146, Amer. Inst. Aeronaut. and Astronaut., New York.
13. J. A. Sethian and A. F. Ghoniem, Validation of the vortex method, submitted for publication.
14. O. Hald, *SIAM J. Numer. Anal.* **16**, 726 (1979).
15. J. T. Beale and A. Majda, *Math. Comput.* **39**, 28 (1982).
16. C. R. Anderson and C. Greengard, *SIAM J. Numer. Anal.* **22**, 413 (1985).
17. Y. Nakamura, A. Leonard and P. Spalart, *AIAA/ASME 3rd Joint Thermophysics, Fluids, Plasma and Heat Transfer Conf., St. Louis, Mo., June* 1982, AIAA–82–0948.
18. A. F. Ghoniem and F. S. Sherman, *J. Comput. Phys.* **61**, 1 (1985).
19. O. Hald, *SIAM J. Sci. Statist. Comput.*, in press.
20. O. Hald, (PAM–270,) *Center for Pure and Applied Mathematics, University of California, Berkeley*, 1985.
21. M. F. McCracken and C. S. Peskin, *J. Comput. Phys.* **35**, 183 (1980).
22. J. A. Sethian, *J. Comput. Phys.* **54**, 425 (1984).
23. E. Acton, *J. Fluid Mech.* **76**, 561 (1976).
24. A. Leonard, *J. Comput. Phys.* **37**, 289 (1980).
25. M. Perlman, *J. Comput. Phys.* **59**, 200 (1985).
26. J. T. Beale and A. Majda, *J. Comput Phys.* **58**, 188 (1985).
27. M. Lighthill, "Introduction: Boundary Layer Theory," *in*: *Laminar Boundary Theory*, L. Rosenhead, Ed. (Oxford Univ. Press, London, 1963), p. 46.
28. R. B. Payne, *J. Fluid Mech.* **4**, 81 (1958).

29. M. K. DENHAM AND M. A. PATRICK, *Trans. Inst. Chem. Eng.* **52**, 361 (1974).
30. B. F. ARMALY, F. DURST, J. C. F. PIERIRA AND B. SCHONUNG, *J. Fluid Mech.* **127**, 473 (1983).
31. H. SCHLICHTING, *Z. Angew. Math. Mech.* **14**, 368 (1934).
32. M. VAN DYKE, *J. Fluid Mech.* **44**, 813 (1970).
33. Y. CAGNON, M. Sc. thesis, Department of Mechanical Engineering, MIT, 1986 (unpublished).
34. R. WESTPHAL, J. P. JOHNSTON AND J. K. EATON, NASA Contractor Report 3765, 1984.
35. F. MILINAZZO AND P. G. SAFFMAN, *J. Comput. Phys.* **23**, 380 (1979).
36. S. ROBERTS, *J. Comput. Phys.* **58**, 29 (1985).